JOURNAL OF SPACECRAFT AND ROCKETS
Vol. 48, No. 1, January–February 2011

Near-Ultraviolet Emission Spectroscopy During an Airborne Observation of the Stardust Reentry

Michael W. Winter* and Kerry A. Trumble†
NASA Ames Research Center, Moffett Field, California 94035

DOI: 10.2514/1.38176

Thermal radiation of the heatshield and the emission of the postshock layer around the Stardust capsule, during its reentry, were detected by a NASA-led observation campaign aboard NASA's DC-8 airborne observatory involving teams from several nations. The German SLIT experiment used a conventional spectrometer, in a Czerny–Turner configuration (300 mm focal length and a 600 lines/mm grating), fed by fiber optics, to cover a wavelength range from 324 to 456 nm with a pixel resolution of 0.08 nm. The reentering spacecraft was tracked manually using a camera with a view angle of 20 deg, and light from the capsule was collected using a small mirror telescope with a view angle of only 0.45 deg. Data were gathered with a measurement frequency of 5 Hz in a 30-s time interval around the point of maximum heating until the capsule left the field of view. The emission of carbon nitride (as a major ablation product), N_2^+ and different atoms were monitored successfully during that time. Because of the nature of the experimental setup, spatial resolution of the radiation field was not possible. Therefore, all measured values represent an integration of radiation from the visible part of the glowing heatshield, and from the plasma in the postshock region. Further, due to challenges in tracking, not every spectrum gathered contained data. The measured spectra can be split up into two parts: 1) continuum spectra, which represent a superposition of the heatshield radiation and the continuum radiation of particles due to microspallation in the plasma, and 2) line spectra from the plasma in the shock layer. Planck temperatures (interpreted as the surface temperatures of the Stardust heatshield) were determined assuming either a constant surface temperature, or a temperature distribution deduced from numerical simulation. The constant surface temperatures are in good agreement with numerical simulations, but the peak values at the stagnation point are significantly lower than those in the numerical simulation if a temperature distribution over the surface is assumed. Emission bands of carbon nitride and N_2^+ were tracked along the visible trajectory and compared with a spectral simulation with satisfying agreement. Values for the integrated radiation of the transitions of interest for these species were extracted from this comparison.

Nomenclature

A_{SMA}	=	area of the lamp exit, m^2
A_{vis}	=	visible Stardust return capsule surface, m^2
c	=	speed of light in vacuum, 299 792 458, m/s
corr	=	correction factor for intensity calibration, μW/counts
conv	=	conversion factor between incident flux and spectrometer response, counts/μW
D_{tel}	=	aperture diameter of the SLIT telescope, m^2
f	=	focal length, m, also factor
f/d	=	ratio of focal length to diameter
h	=	Planck's constant: $6.626\ 10^{-34}$ J s
I	=	intensity, counts
$l_{lamp\text{-}telecope}$	=	distance between SLIT telescope and calibration lamp during calibration measurements, m
$l_{SRC\text{-}DC8}$	=	distance between Stardust return capsule and DC8, km
k	=	Boltzmann constant: $1.3807\ 10^{-23}$ J K^{-1}
L_λ	=	spectral irradiance, W m^{-2} nm^{-1}
M_λ	=	spectral radiance, W m^{-2} sr^{-1} nm^{-1}
n_a	=	numerical aperture
QE	=	quantum efficiency
T	=	temperature, K
T_{Planck}	=	temperature for Planck radiation, K
T_{rot}	=	rotational temperature, K
T_{vib}	=	vibrational temperature, K
α	=	apex half angle, deg
ε_λ	=	spectral emissivity
$\Delta\nu$	=	change in vibrational quantum number during transition
Φ	=	radiant flux, W m^{-2}
Ω	=	solid angle, sr
λ	=	wavelength, nm
$\Delta\lambda_i$	=	wavelength interval for the filter i, nm
τ	=	transmission

Subscripts:

atm	=	atmospheric
EM	=	EMCCD Andor DU971N, charge-coupled device camera used during observation
incident	=	radiation at the DC8 position
i	=	filter number i
lab	=	results during recalibration in the IRS lab
obs	=	results during the observation campaign
OE	=	open electrode, charge-coupled device camera Andor DU920N-OE used during lab experiments for recalibration
pixel	=	charge-coupled device element
scat	=	scattered light
cal	=	calibration data provided by the manufacturer
tot	=	total radiation, that is, sum of UV and scattered light

Presented as Paper 2008-1212 at the 46th AIAA Aerospace Sciences Meeting and Exhibit, Reno, Nevada, 7–10 January 2008; received 21 April 2008; revision received 27 September 2010; accepted for publication 7 October 2010.

*Research Scientist, Optical Plasma Diagnostics, University Affiliated Research Center; Michael.Winter@nasa.gov. Member AIAA.

†Research Scientist, Reacting Flow Environments Branch; Kerry.A.Trumble@nasa.gov. Member AIAA.

I. Introduction

ON 15 JANUARY 2006, after a nearly seven-year celestial journey, the Stardust capsule reentered Earth's atmosphere

with a speed of 12.8 km/s [1]. This was the fastest reentry ever of a human-made space vehicle. Data on heatshield ablation and plasma characterization for this mission would have been very valuable for future sample return missions, e.g., from Mars, which will have similar hyperbolic entry speeds. There were, however, no diagnostics installed in the Stardust capsule to gather data during reentry. Therefore, the only way to obtain information about the heatshield and reentry plasma was through passive optical methods, such as the observation mission led by NASA using the Agency's DC-8 airborne observatory [2]. The observatory flew above the clouds at an altitude of 12 km; absorption in the infrared (IR) is already rather low at these altitudes. However, the ozone layer at altitudes between 25 and 50 km prevented detection of radiation in the UV (i.e., below a wavelength of 300 nm) due to absorption.

The strategy for the observation mission included three test flights before the reentry date, primarily to test the different setups in-flight, and to automate the procedure of mounting the equipment in-flight (equipment had to be disassembled during takeoff and landing). For the final measurement, the airplane was meant to fly three observation loops (each 15 km wide and 45 km long) at an altitude of 12 km above Nevada [3], such that the third time into the straight part of the loop occurred 90 s before reentry (the entry interface was defined as an altitude of 130 km of the Stardust capsule). The difficult task of manual tracking the capsule during the observation period was made easier due to excellent work on preflight prediction of the capsule's trajectory [3], and navigation of the airborne observatory. All scheduled times were met to within 1 s by the DC-8 pilots.

In the observation campaign, a total of 11 different optical experiments were conducted by the American, Japanese, and German teams. These experiments were designed to obtain spectrally resolved data in different wavelength ranges, and with different time resolutions. All spectrally resolving setups used transmission gratings with the exception of a mini Echelle spectrometer [3,4] and the German SLIT experiment which had a conventional spectrometer in a Czerny–Turner configuration ($f = 300$ mm, grating 600 l/mm) fed by fiber optics. The choice of selecting a fiber fed spectrometer for SLIT resulted from the idea to have a spectrometer with a fixed, and rather accurately determined, wavelength range during the whole observation period in contrast to the other experiments which, due to the use of slitless designs with transmission gratings, show a wavelength calibration which depends on the position of the spectrum on the charge-coupled device (CCD) and on the focusing of the optical system. In that sense, the SLIT experiment was meant to provide some spectral fixed point for the transmission grating measurements. In addition, SLIT was supposed to gather spectral data with high resolution as far as possible towards the UV. As a trade off, tracking was a major challenge for the SLIT experiment because the view angle of the telescope was limited to 0.45 deg to focus on the optical fiber bundle. Data were taken with a measurement frequency of 5 Hz during a 15 s time interval on either side of the point of maximum heating until the capsule left the field of view. Because of difficulties in tracking, not every spectrum contained data.

The spectra contain a superposition of continuum spectra from heatshield radiation and particles due to microspallation of the heatshield material in the plasma [5,6], and line spectra from the plasma in the shock layer. The contribution of each of these sources of radiation has to be separated during the data evaluation process. None of the setups was able to resolve the emitted radiation spatially. Therefore, all measured data are integrated over the visible part of the glowing heatshield and over the plasma in the postshock region.

During postflight calibration of SLIT, a major effect of scattered light due to thermal emission in the visible and near infrared was seen which was found to be wavelength dependent and therefore temperature dependent for Planck radiation. This meant that scattered light was different for different Stardust temperatures and a conventional calibration would have to be corrected for each single spectrum by the (unknown) surface temperature. Therefore, a different approach for the determination of Stardust return capsule (SRC) surface temperatures was chosen in simulating the spectral response of the spectrometer due to thermal radiation. and iteratively finding The best match of this simulated spectrometer response in comparison to the raw data by iteratively varying the simulated temperature was considered as the measured SRC surface temperature. By subtracting this iteratively found thermal emission from the measured spectra, the plasma spectrum was obtained which could be calibrated by a conventional intensity calibration.

In the following, the setup of the SLIT experiment is described in detail. The evaluation process, including the simulation of the spectrometer response to thermal radiation, the separation of continuum from line spectra, and the calibration of the measurement for plasma radiation is presented. For a better comparison with numerical results, some generalized shape for a temperature distribution of the SRC surface temperature was extracted from computational fluid dynamics (CFD) data although no temperature values were introduced to keep the data analysis independent from theoretical simulation. The CFD solution is introduced and the interpretation of the measured spectra yielding Planck temperatures determined from the measured continuum spectra is compared with the CFD data and to data from other experiments.

II. Experimental Setup and Data Acquisition

The SLIT experiment joined the observation campaign rather late in October 2005. Therefore, design, manufacture, and calibration of the whole experimental setup had to be completed within three months with very limited funding. An Acton 300i spectrometer with a focal length of 300 mm was used. For detection, an Andor DU971N EMCCD camera with 1600×400 pixels of an individual size of 16×16 μm was used. The EMCCD technology enables charge from each pixel to be multiplied on the sensor before read out, providing single photon sensitivity with both multi-Megahertz readout and USB connectivity.[‡] After trials with different gratings, a 600 l/mm grating was chosen for use in the wavelength range between 324 to 456 nm with a pixel resolution of 0.08 nm. Because of the lack of light during the observation, the spectrometer slit was kept open to collect the largest possible amount of light. Therefore, the fiber diameter was imaged on up to six fibers yielding a final instrument broadening with a full width at half maximum (FWHM) of 0.3 nm.

A reflector telescope was used to focus on the Stardust capsule. Since the usable diameter of the optical fiber was limited by the necessity to feed the radiation into the spectrometer with a small equivalent slit width, the design options for the focusing optics were rather limited. The setup was designed to maximize the view angle under which radiation would be focused on the fiber optics. This constraint required a focal length as small as possible and a fiber diameter as large as possible. On the other hand, the fiber diameter had to be as small as possible to improve spectral resolution and losses at the entrance of the spectrometer. The f/d ratio of the optics was limited to roughly 2 by the numerical aperture of $n_a = 0.22$ of the fiber optics. Finally, an off-axis parabolic mirror with an equivalent focal length of 100 mm and a diameter of 50 mm was chosen. The contradicting requirements for the optic fibers at the telescope and the spectrometer side were resolved using a bundle of 50 fibers with 100 μm diameter each. At the telescope exit they were fixed in a round configuration yielding an overall fiber diameter of 0.6 mm and hence, a view angle of 0.45° (which corresponds approximately to the visible size of the moon). At the spectrometer entrance the fibers were reoriented into a linear row forming an equivalent entrance slit with an effective slit width of less than 100 μm. If sufficient light intensity would have been available (which unfortunately was not the case), this slit width could have been further reduced by the mechanical entrance slit of the spectrometer. A spatial assignment of a single fiber in the round cross section to a vertical position in the equivalent slit was not possible due to manufacturing constraints. Therefore, light which hit somewhere in the round cross section was displayed at an arbitrary position on the entrance slit. Since spatial resolution of the Stardust capsule was not possible anyway, for detection, the principle of full

[‡]Product information available online at http://www.andor.com [accessed Oct. 2010].

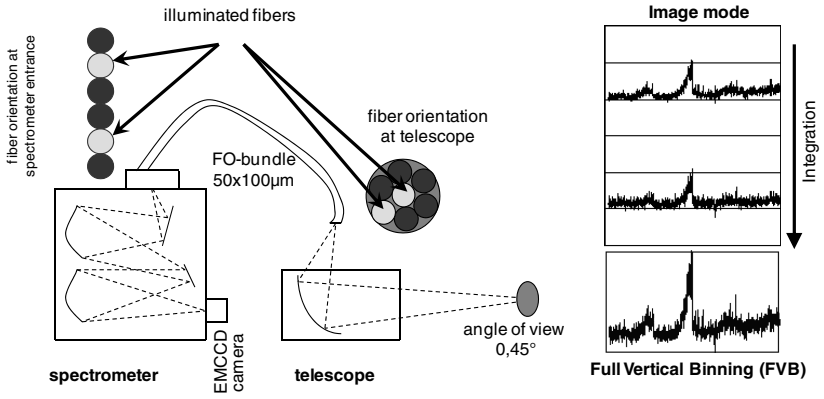

Fig. 1 Principle design of the SLIT experiment with an illustration of the full vertical binning mode.

vertical binning (FVB) was chosen. Here, all CCD rows are integrated in hardware and are displayed as a single spectrum. Then again, noise is reduced in general and signal to noise ratio is improved remarkably by this approach. Figure 1 illustrates the combination of telescope, fiber optics, and spectrometer and the full vertical binning mode which was used during data acquisition.

The view angle of 0.45° required an optical aide to permit successful manual tracking. Unfortunately, an automatic system with feedback was not available. Therefore, a conventional video camera was used to tape the screen of a light intensifier with a Canon lens system (focal length 100 mm, $f/2.0$) with a viewing angle of roughly 20° to help with the manual tracking. The intensifier was rigidly connected to the mount of the telescope so that a defined relation between the two viewing angles was granted. Figure 2 shows the combined setup mounted on a ball mount close to the window of the airplane. A grid was glued to the intensifier screen which enabled an assignment of the detected spot of the spectrometer telescope combination to the video. Figure 3 shows an image of the nightly sky taken during the final observation. The intensifier was strong enough to see the stars in the sky. The constellation Pleiades is clearly seen in the picture. The area detected by the spectrometer is marked by a red dot and was determined using measurements of the moon taken on the tarmac.

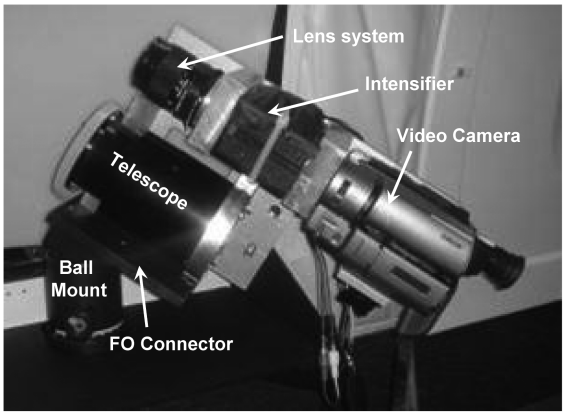

Fig. 2 SLIT optics on the ball mount.

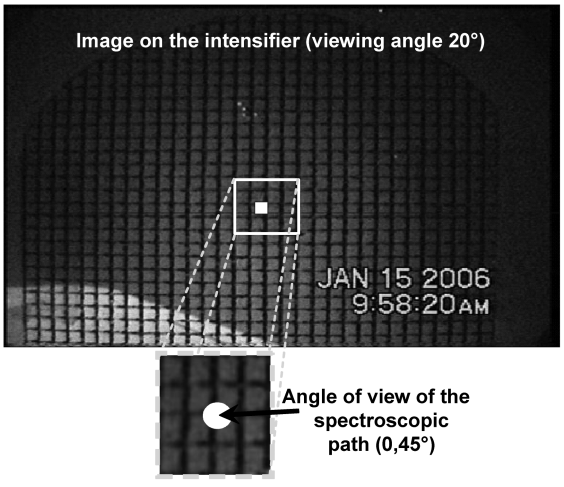

Fig. 3 Video image for manual tracking assistance.

During the observation, spectra were taken with an acquisition time of 0.2 s and a repetition frequency of 5 Hz. Even with this setup, tracking was still rather difficult. It turned out that during data acquisition, not every spectrum contained data because the image of the capsule was not always fully captured by the optical fiber. Consequently, the overall intensity showed fluctuations, too, when the fiber bundle was only partly illuminated. Only the spectra with the maximal intensity are used for the part of the evaluation that requires absolute intensity information. Although the telescope and the intensifier were rigidly connected to the common base plate, it turned out that the video camera was able to move slightly. Therefore, the point of data acquisition shows slight movements on the video image which was to be taken into account during evaluation. Stardust data was acquired during about 30 s of the reentry starting at Stardust altitudes of about 84 km over ground down to altitudes of 45 km.

III. Data Reduction and Calibration

Before the data could be analyzed, the raw data had to be corrected for dark current, and cosmic rays needed to be removed. In a second step, the time-correlated data had to be compared with the video image to determine where the capsule was detected in the field of view (e.g., before, behind, or directly on the capsule). The spectral data had to be wavelength and intensity calibrated. Because of strong effects of scattered light, a direct calibration of the thermal continuum part of the measured spectra could not be performed. Instead, a simulation of the spectrometer response to thermal radiation was developed. Finally, the atmospheric influences (i.e., absorption) had to be taken into account. For this purpose, the horizontal and vertical distances between airplane and Stardust are needed. For the further interpretation of the data, even the orientation of the Stardust capsule relative to the airplane had to be known to calculate the thermal radiation to be measured at the DC8 position. These different procedures are described in the following subsections.

A. Subtraction of Dark Current and Cosmic Rays

On the airplane, the occurrence of cosmic rays was significantly higher than on ground. Because of the high sensitivity and amplification of the camera emission lines due to cosmic rays are of intensity comparable to that of true emission lines. Fortunately, these lines appear only on one camera pixel, which is much narrower than plasma emission lines, which are broadened by the optical components to a full width at half maximum of 4 pixels. Therefore,

lines due to cosmic rays could be identified and were eliminated from the measured spectra.

The background correction was complicated by a hot pixel column at pixel 997, which corresponds to a wavelength of 406.6 nm. After binning and amplification, this column produced a disturbing emission 10 times higher than the highest emission from Stardust. However, a spectrum taken before Stardust was visible was used as background [7].

B. Spatial Assignment of Measured Position Relative to the SRC

Although no spatial resolution of the capsule is possible, the position of the sensitive spectrometer field of view in the video image is needed to find out if the corresponding spectrum resulted from the SRC being in the center or at the edge or even outside this field of view. However, when moving the setup on the track ball, the video camera occasionally moved (slightly) against the base plate where the intensifier and the telescope were mounted. Therefore, a fixed point on the intensifier screen was not always in the same position on the CCD array. A computer routine was developed to apply corrections to compensate for this movement. Groups of pixels were selected for integration and displayed vs time. The result was compared with the sum over all pixels of the measured spectra. The best qualitative match between these two curves gives the pixels on the video which correspond to the spot measured by the telescope. Indeed, some spectra were taken while the SRC was at the edge of the field of view, some even in the wake. If the tracking is off, the signal can only weaken. Furthermore, a continuous variation of the signal strength is expected rather than sudden jumps. Therefore, the points where tracking was found to be sufficiently good were connected by a compensating curve. The difference of the actual measurements to this curve is considered to characterize the uncertainty due to imperfect tracking and will be used later to specify temperature uncertainties due to tracking. Figure 4 displays the best match of the integration inside the video and the total intensity on the EMCCD. Note that a perfect match should not be expected because intensity in the video image is affected by masking of the intensifier by the grid lines.

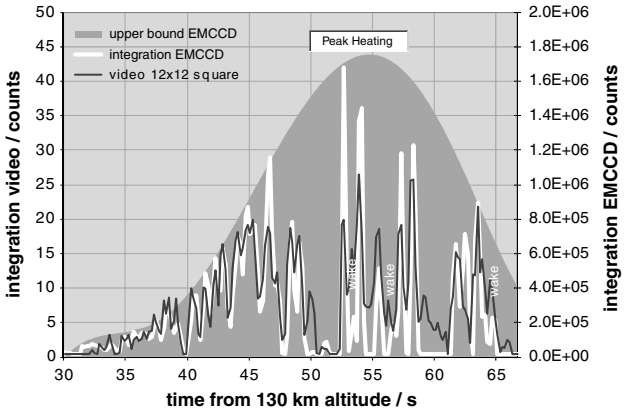

Fig. 4 Integration over the measured position in the video image and total intensity on the EMCCD vs time and estimates of the upper bound for the spectral measurements (*wake* specifies spectra where the center of field was behind the capsule). Higher peaks show stronger signal and therefore indicate the SRC centered in the field of view, lower peaks indicate that the tracking is off.

C. Wavelength and Intensity Calibration

Wavelength calibration was performed by measuring the emission of a Mercury lamp. The calibrated wavelengths were then obtained from a second-order polynomial fit. For intensity calibration, a calibration lamp (Ocean Optics LS1) was placed in a distance of $l_{\text{lamp-telecope}} = 3.86$ m to the telescope. The intensity L_{LS1} was given in $\mu\text{W}(\text{cm}^2\ \text{nm})$ for an optical fiber directly connected to the lamp port. This intensity was converted to spectral radiance using the numerical aperture of a typical fiber of $n_a = 0.22$. Obviously, this distance is significantly different from the distance to the Stardust capsule, which varied between 440 and 70 km during the measurement period in-flight. Furthermore, both solid angle and atmospheric transmission varied, too. Therefore, a calibration to radiant power rather than to radiance was carried out. The calibration values were transformed to radiant power at the entrance of the telescope using the distance between lamp and telescope in combination with the telescope aperture diameter. Finally, this value was integrated over the wavelength interval covered by each pixel. During data evaluation, discrepancies between simulated and measured spectra were observed showing inconsistent ratios between the $\Delta v = 0$ and $\Delta v = -1$ bands if the band shape at $\Delta v = 0$ was correctly reproduced [7]. This inconsistency pointed to a problem in the calibration. Therefore, recalibration measurements were carried out. It soon became obvious that the calibration was heavily influenced by scattered light inside the spectrometer. The measurement took place in the UV, but the calibration lamp used has its emission maximum between the visible (VIS) and the near infrared (NIR) range. This radiation, which is higher than the UV radiation by at least 3 orders of magnitude, was improperly processed by the spectrometer and appeared at the CCD as scattered light. Whenever the expression *scattered light* is used in the following, it refers to this process. Figure 5 shows a measurement of a similar calibration lamp (Ocean Optics LS1) with and without an edge filter (Schott GG495) which blocks radiation across the whole measured range. The difference between these measurements gives the lamp emission corrected for scattered light. Unfortunately, the EMCCD camera (Andor DU971N UVB) which was used for the observation mission was not available for the recalibration. Therefore, the recalibration was done with an Andor DU920N OE camera, which uses a CCD chip with the same over all dimensions as in the EMCCD. This similarity in dimensions means that the geometrical factors on scattered light are maintained in between the recalibration and the observation. The spectral quantum efficiencies of the two cameras, however, were substantially different as shown in Fig. 5. These manufacturer's data were used to extrapolate the scattering results from the one camera to the other.

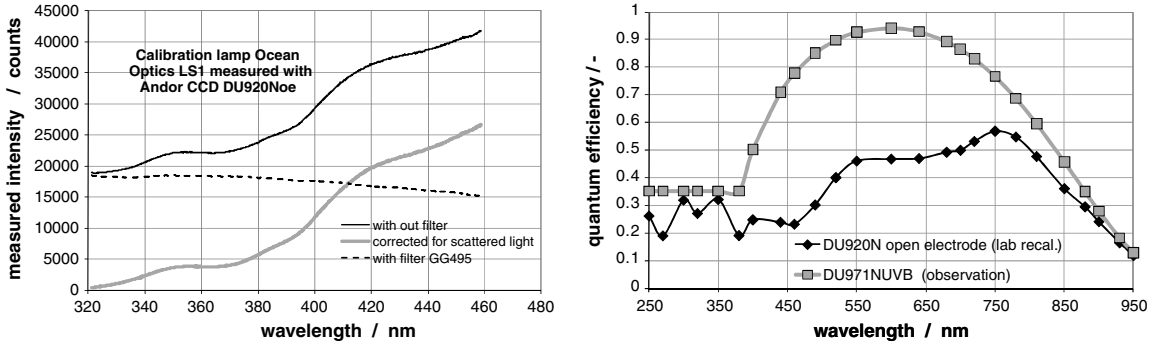

Fig. 5 Calibration lamp Ocean Optics LS1 measured with CCD camera Andor DU920N open electrode with and without edge filter GG495 and quantum efficiencies of the two cameras used.

The amount of scattered radiation is a function of only the spectrometer, the grating and the fiber optics were not changed. In the measured range (i.e., 324–456 nm) the ratio of the quantum efficiencies was used for conversion. The spectral composition of the scattered light is unknown a priori, and varies for different positions on the CCD array (which again correspond to different wavelengths). Therefore, measurements with a series of edge filters (edges at wavelengths 495, 515, 535, 550, 570, 590, 610, 630, 645, 665, 695, 715, 780, 830, and 850 nm) were made to estimate the spectral composition of the scattered light from the differences between the single spectra. Above wavelengths of 1000 nm, the sensitivity of both cameras drops down drastically. The main contributions were found to be from radiation between 600 and 850 nm.

In the following, the recalibration measurements are referred to by the suffix *lab*, the results with the different cameras are labeled *OE* (open electrode) for the DU920N and *EM* for the DU971N, the measurements during and after the observation are marked by the suffix *obs*. The goal of these measurements was to obtain a scaling factor between measured emission (with and without scattered light) to be applied to the calibration measurements which were taken during the observation campaign. The terms wavelength and pixel do appear simultaneously in some equations to accentuate the pure dependence on wavelength (e.g., the calibration lamp emission in the UV) and the additional dependence on geometry (i.e., the position on the CCD) where one pixel is affected by radiation from different wavelengths. The measured intensity is the sum of scattered light and UV emission:

$$I_{\mathrm{LS1,tot,lab,OE}}(\mathrm{pixel}) = I_{\mathrm{LS1,UV,lab,OE}}(\lambda) + I_{\mathrm{LS1,tot,lab,OE}}(\mathrm{pixel}, \Delta\lambda_i) \tag{1}$$

$I_{\mathrm{LS1,UV,lab,OE}}$ is a function of wavelength only (and not of geometry), the conversion from the OE (open electrode) camera to the EMCCD of the UV emission is done by a multiplication with the ratio of the quantum efficiencies, which are also functions of wavelength:

$$I_{\mathrm{LS1,UV,lab,EM}}(\lambda) = I_{\mathrm{LS1,UV,lab,OE}}(\lambda) \qquad \mathrm{QE_{EM}}(\lambda)/\mathrm{QE_{OE}}(\lambda) \tag{2}$$

$I_{\mathrm{LS1,scat,lab,OE}}$ depends on geometry and therefore on the pixel position on the CCD and on the true wavelength of the scattered light which is approximated by the combinations of measurements with different edge filters in the wavelength intervals $\Delta\lambda_i$. The contribution of scattered light to the measurement without filter is the sum of all differential measurements with the edge filters, each of them multiplied by the ratio of quantum efficiencies in the wavelength range of concern:

$$I_{\mathrm{LS1,scat,lab,EM}}(\mathrm{pixel}) = \sum_i I_{\mathrm{LS1,scat,lab,OE}}(\mathrm{pixel}, \Delta\lambda_i) \qquad \mathrm{QE_{EM}}(\Delta\lambda_i)/\mathrm{QE_{OE}}(\Delta\lambda_i) \tag{3}$$

The desired relation is then:

$$f_{\mathrm{LS1,UV,EM}}(\mathrm{pixel}) = \frac{I_{\mathrm{LS1,UV,lab,EM}}(\lambda)}{I_{\mathrm{LS1,UV,lab,EM}}(\lambda) + I_{\mathrm{LS1,scat,lab,EM}}(\mathrm{pixel})} \tag{4}$$

If $f_{\mathrm{UV,EMCCD}}$ is multiplied with the measured emission of the LS1 lamp during observation the results should be the true emission in the UV range:

$$I_{\mathrm{LS1,UV,obs,EM}}(\lambda) = f_{\mathrm{LS1,UV,EM}}(\mathrm{pixel})\ \ I_{\mathrm{LS1,tot,obs,EM}}(\mathrm{pixel}) \tag{5}$$

If applied to the calibration measurement during the observation, the reconstruction using the above ratios does only match the measured emission below 400 nm if the scattered light is increased by 35%. For reasons unknown, the amount of scattering seemed to have changed during the observation and the recalibration. The level of confidence of the postflight lab calibration is somewhat higher due to present data with and without spectral filters, but the measurements during the observation campaign were conducted with the original CCD. Therefore, all following analyses have been performed both with the original values for scattered light from the lab measurements and with a value increased by 35%, to get an idea of the uncertainties introduced by this variation rather than just taking the average value and consider error bars of $\pm 17.5\%$. As will be shown later, the effect on the Planck temperatures to fit the measured data is rather small due to the shape of the Planck curve.

One consequence of this strong effect of scattered light is that thermal emission of the capsule surface cannot be captured by a straight forward calibration since the spectral distribution in the VIS/NIR wavelength region will change with the surface temperature. The above shown correction is a priori only valid for the spectral distribution of the calibration lamp. The calibration factor for thermal emission of the SRC surface would therefore depend on the (unknown) surface temperature. Rather than redefining the calibration factor for each SRC position, a spectrometer response to thermal radiation was simulated and fitted to the raw data. This procedure is described in the data analysis chapter. The following calibration procedure was only used for the pure plasma spectra after subtraction of Planck emission. Here, the effect of scattered light from plasma emission in the VIS and NIR would be in the noise level of the measured data if the plasma emission is lower than the thermal radiation by 1 order of magnitude which, to the opinion of the authors, justifies a straight forward calibration approach.

For calibration of the true UV radiation, the ratio of the UV portion of the calibration measurement and the calibrated radiance of the lamp $L_{\mathrm{LS1,cal}}$ provided by the manufacturer is used. Therefore the effect of scattered light is considered negligible. Following the procedure described at the beginning of this section, the original calibration curve was converted from the calibration units $\mu\mathrm{W/cm^2}$ nm to an incident radiant power in μW by:

$$\Phi_{\mathrm{LS1,incident}}(\lambda) = L_{\lambda,\mathrm{LS1,cal}}(\lambda)\ \ A_{\mathrm{SMA}} \frac{\Omega_{\mathrm{tel}}}{\Omega_{\mathrm{LS1}}} \Delta\lambda_{\mathrm{pixel}} \tag{6}$$

where A_{SMA} is the area of the lamp exit, Ω_{LS1} is the solid angle in which the lamp radiation is emitted, determined from the numerical aperture $n_a = 0.22$ given by the manufacturer, Ω_{tel} is the solid angle from which the telescope receives radiation, determined from the geometry, and $\Delta\lambda_{\mathrm{pixel}}$ is the wavelength width of each pixel.

A correction factor is obtained to:

$$\mathrm{corr}_{\mathrm{LS1,UV,EM}}(\mathrm{pixel}) = \frac{\Phi_{\mathrm{LS1,incident}}(\lambda)}{I_{\mathrm{LS1,UV,obs,EM}}(\lambda)} \tag{7}$$

Figure 6 shows the obtained calibration factors with and without correction for scattered light as well as the calibrated curve provided by Ocean Optics. This calibration curve combined with the atmospheric extinction was used for the calibration of the plasma spectra.

D. Simulation of the Spectrometer Response to Planck Radiation

As mentioned before, the measurements of Planck radiation from the SRC surface are contaminated by scattered light. The amount of scattered light depends on the spectral distribution in the VIS and NIR range, which varies with the underlying surface temperature. Therefore, the factors for scattered light will change with SRC

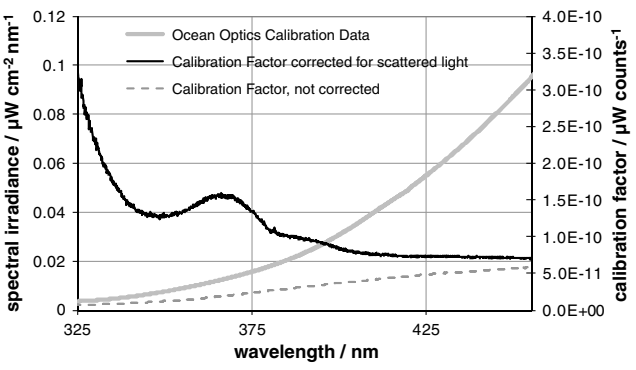

Fig. 6 Ocean Optics calibration data and SLIT calibration factor.

surface temperature. As a consequence of this variation, separate determination of scattered light had to be performed for each single spectrum. A uniform calibration was not possible for the thermal radiation since the underlying Planck temperatures were not known. Rather than converting the measured signal to radiant power, the simulated Planck emission of the SRC surface was converted to counts measured by the spectrometer system giving a simulated spectrometer response to any assumed Planck radiation including the effects of scattered light. Again, the measurements of the LS1 calibration lamp with the edge filter combinations were used. For each wavelength interval $\Delta\lambda_i$, the product of the calibrated intensity $L_{\lambda,\mathrm{LS1,cal}}$.in $\mu\mathrm{W/cm^2\,nm}$ provided by the manufacturer and the combined transmission of the filter combination of concern was integrated over wavelength:

$$L_{\mathrm{LS1,cal}}(\Delta\lambda_i) = \int L_{\lambda,\mathrm{LS1,cal}}(\lambda)\{\tau_i(\lambda) - \tau_{i-1}(\lambda)\}\,\mathrm{d}\lambda \tag{8}$$

and converted to incident radiant power $\Phi_{\mathrm{LS1,incident,obs}}(\Delta\lambda_i)$ as described above. For the UV radiation, the correction factor for intensity calibration is inverted. Thus, conversion factors are obtained to:

$$\mathrm{conv}_{\mathrm{theory,scat,obs}}(\mathrm{pixel}, \Delta\lambda_i) = \frac{I_{\mathrm{LS1,scat,obs,EM}}(\mathrm{pixel}, \Delta\lambda_i)}{\Phi_{\mathrm{LS1,incident,obs}}(\Delta\lambda_i)} \tag{9}$$

$$\mathrm{conv}_{\mathrm{theory,obs}}(\lambda) = \frac{1}{\mathrm{corr}_{\mathrm{LS1,UV,EM}}(\mathrm{pixel})} = \frac{I_{\mathrm{LS1,UV,obs,EM}}(\lambda)}{\Phi_{\mathrm{LS1,incident}}(\lambda)} \tag{10}$$

in [counts/μW]

These conversion factors are used to transform incident radiant powers into a simulated spectrometer signal. To account for the observed uncertainty in the amount of scattered light, all analyses are conducted both for the above shown value and the one increased by 35%. For the following analysis of the measured spectra, thermal radiation emitted by the SRC heatshield at a given temperature is computed and corrected for distance, solid angle, SRC orientation (i.e., effective emitting area) and atmospheric extinction until an incident thermal radiation at the telescope position is received. This incident thermal radiation is converted into an equivalent spectrometer response and compared with the measured raw data. The underlying Planck temperature distribution for the best fitting spectrum is considered as the desired solution. The plasma spectrum is then extracted as the difference between measured spectrum and simulated response to the best fitting Planck radiation. In the following, the different influences on the SRC radiation will be discussed and the method of generating the simulated thermal radiation will be shown.

E. Atmospheric Transmission

For a conversion of radiation emitted by Stardust (i.e., Planck and plasma radiation), it must be multiplied with the corresponding solid angle obtained from the distance, the emitting surface area or plasma volume, and with the corresponding air transmission. The spectral transmission of the atmosphere as shown in Fig. 7 was computed using the ModTran code [8,9] using aerosol and ozone concentration as input parameters. Assuming aerosol concentration to be normal, ozone concentration was determined to 300 DU (Dobson units) from ozone maps from the World Ozone and Ultraviolet Radiation Data Centre provided by the Environment Canada on the internet for the reentry day of Stardust.

F. Visible Surface and View Factors

To quantify the Planck radiation received at the airborne observatory, the visible surface of the Stardust capsule and the distribution of the angle between the surface normal vector and the optical axis to the DC8 must be known for each surface element. The position and orientation of the DC8 observation aircraft are known from GPS data, and the Stardust capsule position is taken from the trajectory data. For the orientation of the Stardust capsule it is assumed that the vehicle axis is oriented in direction of the velocity vector which is extracted for each altitude from the difference of two successive trajectory points. If these data sets are combined, the distances and view angles as depicted in Fig. 8 are obtained. The view angle is defined to be 0° if the observation axis coincides with the vehicle axis (view from the front), and 90° if the vehicle is observed at right angles to the flight vector (side view). The maximal angle during the observation period was about 50° at an altitude of 49 km. The surface has been calculated as a sphere with a radius of 0.22 m up to an angle of 30.5° and a truncated cone with a cone angle of 30.5° up to an outer radius of 0.405 m. Because of this shape of the Stardust capsule, the whole heatshield surface of 0.5947 $\mathrm{m^2}$ is completely visible to a maximum angle of 59.5°. However, according to Lambert's Law the detected intensity of a radiating surface is proportional to the cosine of the angle under which the surface is observed. Therefore, the detected intensities decrease with this angle, thereby yielding an increase in the deduced Planck temperature. This effect is covered by the view factor. For the assumption of a constant surface temperature, integration over the whole surface yields an average view factor for each altitude as depicted in Fig. 8. If a temperature distribution is applied, the integration has to be done over the product of locally emitted Planck radiation with the local viewing factor at each surface position. Images of the SRC in its orientation to the DC8 are added to Fig. 8.

IV. Simulation of the Stardust Reentry and Approximation of a Generalized Surface Temperature Distribution

Results from a simulation of the flowfield and the resulting surface temperatures using CFD and a material response code are used for a

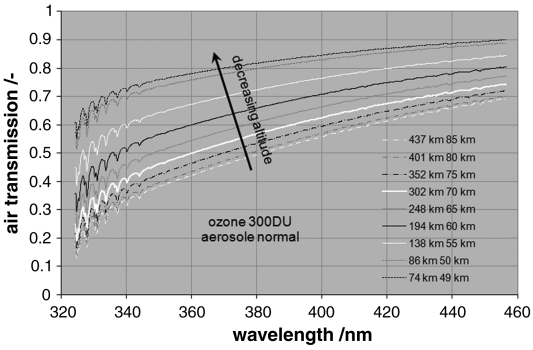

Fig. 7 Atmospheric transmission between DC8 and Stardust for different Stardust altitudes.

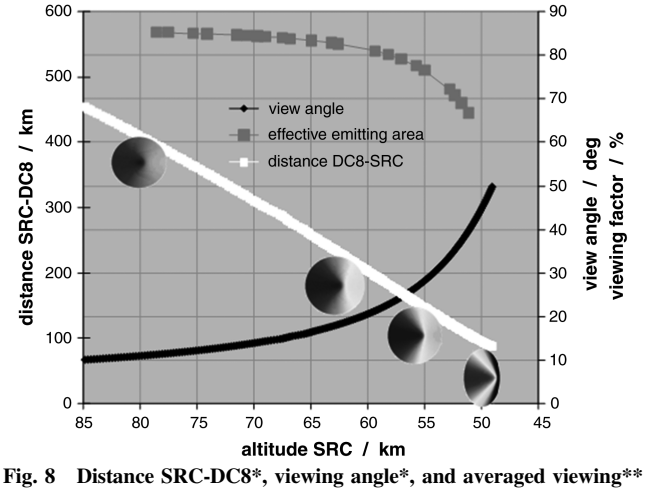

Fig. 8 Distance SRC-DC8*, viewing angle*, and averaged viewing factor vs SRC altitude (*: according to Nominal Entry Trajectory Data: s06015f [18], **: this work).**

comparison with the results from the measurement campaign to be shown in the last chapter. Although the analysis of the experimental data was performed completely independent from CFD simulation or other results from other experiments, the qualitative distribution of the surface temperature was adapted from the CFD simulation for the sake of consistency. Therefore, the basics of the CFD simulation and the derived approximation of qualitative surface temperature are presented here before the final analysis of the experimental data is presented.

A. Flowfield

The method of analysis for the thermal protection system begins with computation of the flowfield at several time points (to sufficiently capture the heat pulse) along the estimated flight trajectory (EFT). For the present work, flowfields solutions along the EFT were calculated using the CFD code DPLR (data parallel line relaxation). DPLR is a parallel, multiblock, finite volume code that solves equations governing the continuum flow of a mixture of gases in chemical and thermal nonequilibrium. The Euler fluxes are computed using modified Steger–Warming flux vector splitting [10] with third-order spatial accuracy via MUSCL extrapolation [11]. The viscous fluxes are computed to second-order accuracy using a central-difference approach. The flow is assumed laminar, in thermochemical nonequilibrium, and is modeled with a two-temperature, 11 species (N_2, O_2, NO, NO_2, N_2^+, O_2^+, N, O, N^+. O^+, and e^-) and 19 reactions finite-rate air chemistry model. Vibrational relaxation is based on the Landau–Teller formulation; relaxation times are obtained from Millikan and White [12], assuming a simple harmonic oscillator model, with the high-temperature correction of Park [13]. Rotational relaxation is based on the Parker model [14]. Viscous transport and thermal conductivity are determined using the mixing rules of Gupta et al. [15]. The species diffusion coefficients are calculated with a bifurcation model [16], which has been shown to compare well with exact solutions of Stefan–Boltzmann equations [17]. The surface of the heatshield is assumed to be in radiative equilibrium with a constant emissivity of 0.85. Furthermore, the wall is assumed fully catalytic with a catalytic efficiency of 1.0 for atom recombination; the wall was assumed fully catalytic to ions as well.

Because Stardust is an axisymmetric configuration, and its entry trajectory was ballistic [18], flowfield analyses can be performed using a two-dimensional axisymmetric grid, thereby saving computational resources. The grid used in the present work was composed of six blocks and 43,000 grid cells. The grid was grown out hyperbolically in the body-normal direction and orthogonality of grid lines at the surface was ensured. As the solution converged on the hyperbolic grid, the grid was then tailored to achieve good alignment of the outer boundary with the bow shock.

Because high-fidelity CFD computations are performed only at a finite number of time points on the EFT, aerothermal environments along the entire trajectory are constructed using a combination of CFD and engineering scaling relationships. Between CFD solutions, environments are linearly interpolated in time using the CFD results. At trajectory points outside the time interval considered for CFD, areothermal environments are determined using scaling relations based on freestream velocity and density (i.e., enthalpy scales with v^2, heat transfer coefficient scales with ρv, and pressure scales with ρv^2). Scaling will vary spatially over the heatshield. Therefore, each surface point is scaled separately to provide heating pulse continuity in time.

B. Material Response

In the present analysis, phenolic impregnated carbon ablator (PICA) material response along the Stardust EFT is modeled using version 2.4 of FIAT [19], and Version 3.3 of the PICA model [20]. The aerothermal environment (recovery enthalpy, pressure and heat transfer coefficient) along the trajectory, as determined from CFD simulations is input into FIAT. In the present analysis, the contribution of shock-layer radiation is not included since it accounted for less than 10% of the heat rate at peak heating, and surface heating was dominated by convective heating [21]. Next, the surface energy balance equation that accounts for conduction, blowing, pyrolysis and surface recession is solved. The material stack consists of PICA (5.8 cm), HT-424 (0.14 cm) and aluminum 2024 (1.27 cm) and a planar geometry is employed. All materials have an assumed initial temperature of -20°C. There is no contact resistance at any material interface and the back wall is assumed adiabatic. The properties (heat capacity, thermal conductivity, emissivity) of the material in the thermal protection system stack are read in from the FIAT material database. Heat capacity is modeled as a temperature dependent quantity, while thermal conductivity varies with both pressure and temperature. For ablators, these material properties are separately listed for virgin and char material. Within FIAT, the emissivity of PICA for both virgin and char is modeled as temperature dependent and varies from 0.858 at 250 K to 0.93 at 3500 K.

The iteration between CFD and FIAT is loosely coupled, the surface temperatures returned by FIAT are put back as a point-by-point isothermal boundary condition into the DPLR CFD code, and a flowfield solution is recomputed. This loosely-coupled iterative procedure is deemed converged when the differences in heat fluxes from two successive cycles of DPLR-FIAT iterations are within 5% [22].

C. Approximation of a Temperature Distribution over the Heat Shield

To provide a temperature distribution for the analysis of the experimental data, the real distribution is approximated as a combination of two linear distributions. The shape of this combination was obtained from an analysis of temperature distributions from CFD simulations using DPLR. However, the input from the CFD simulation was intended to be kept to a minimum to maintain the autonomy of the experimental data analysis. For this purpose, all CFD-predicted temperatures were normalized by the value at the apex of the heatshield (also the stagnation point), and a normalized CFD distribution was approximated by two straight lines which intersect at an axial location of 5 cm approximately from the apex. This distribution matched the CFD solution on the spherical part of the heatshield close where the highest surface temperatures (consequently the highest contribution to thermal radiation) were predicted. However, the distribution does show deviations at larger distances from the tip of the capsule. At this part of the surface, the simplified distribution overpredicts the DPLR temperatures at high altitudes and underpredicts them at lower altitudes. If the same radiative flux has to be reproduced this would yield lower experimental temperatures at early reentry and higher values at the end of the observation period. Note that only the shape of the distribution is adapted from DPLR solutions. No temperature values

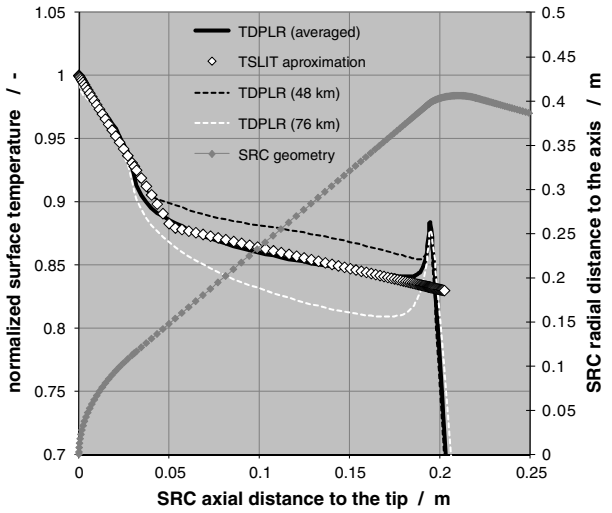

Fig. 9 Assumed SRC temperature distribution in comparison to normalized DPLR results. The normalized DPLR temperatures are shown as an average over observation period as well as early and late in the trajectory where the departures from this average were maximal.

are interchanged, thus keeping the data analysis independent of the CFD solution. For the analysis, the SRC tip temperature was varied and the temperatures across the surface were computed according to this approximation, assuming rotational symmetry. Figure 9 shows the assumed temperature distribution in comparison to the normalized DPLR results. A consistency check between the two cases of constant and varying surface temperature to prove the integration procedure over the surface has been performed by reproducing the thermal emission for a constant surface temperature if a flat line with corresponding temperature was chosen as input.

V. Data Analysis and Interpretation

The measured spectra are a superposition of shock-layer radiation, and continuous radiation emitted by the glowing heatshield. Because of the strong effect of scattered light, a straight forward calibration cannot be applied to the thermal emission as already discussed in Sec. III. Instead, a temperature is assigned to the capsule surface and the emitted thermal radiation is computed as gray body radiation. Then, the irradiance at the telescope entrance is determined taking into account the visible surface area, the atmospheric losses, and the effective solid angles according to the distance of the SRC to the airborne observatory. Finally, the simulated spectrometer response to that irradiance including scattered light according to the method explained in Sec. III is computed. This spectrometer response is compared with the measured spectra in CCD counts and the assumed surface temperature is iterated until best agreement with the measured spectrum is achieved. The spectrum was considered to be in best agreement when the thermal continuum radiation seemed to be eliminated from the shape without driving the resulting plasma spectrum to negative values. The originating temperature (or temperature distribution) is considered the experimentally determined surface temperature. The plasma radiation is obtained by subtracting this thermal emission from the measured spectrum. The resulting plasma spectrum is calibrated using the calibration procedure described in Sec. III.C. The total spectrum at this trajectory point is reconstructed as the sum of calibrated plasma emission and theoretically determined irradiance at the DC8 position. This procedure is repeated for each trajectory point with significantly high measured intensity.

As a first step in the data evaluation process, the heatshield temperature is assumed constant. In reality, this assumption is tenuous because temperature varies across the surface of the heatshield, as do the plasma composition and temperatures across the shock layer. Therefore, in a second step, a surface temperature distribution based on CFD simulations as described in Sec. IVis used. It should be noted that the ablation process most likely causes particles to be injected into the flow. These material particles themselves emit continuum radiation due to their surface temperature [5,6]. However, without any further information about the size and loading of the particles in the shock layer nothing further can be done because there are too many free parameters to obtain a single solution. Possible improvements of the evaluation procedure to relax these restrictive simplifications are discussed later.

A. Estimation of Heat Shield Temperatures

Two cases 1) of constant SRC surface temperature over the heatshield for the entire flight trajectory, and 2) a predefined temperature distribution (piecewise linear variation as described in the previous section) are investigated in parallel. Both cases are at best approximations to the real distributions because of these simplifying assumptions.

The spectral radiance from the glowing heatshield was calculated according to Planck's formula for a gray body is given by:

$$M_\lambda(T) = \varepsilon_\lambda \frac{2\pi hc^2}{\lambda^5} \frac{1}{\exp(\frac{hc}{\lambda kT}) - 1} \tag{11}$$

The emissivity of PICA was assumed independent of wavelength since no such spectral data are available. Temperature dependent emissivity data for PICA after arc jet testing are available only for temperatures below 1900 K [23]. Above 1920 K the emissivity was assumed to be constantly 0.9.

The spectral radiance was first integrated to the wavelength widths of the different CCD pixels and then multiplied by the visible surface area, the atmospheric transmission already shown in Fig. 7, and the solid angle:

$$\Omega = 2\pi(1 - \cos\alpha) \tag{12}$$

where the apex half angle

$$\frac{\alpha}{2} = \arctan\left(\frac{D_{\text{tel}}}{2L_{\text{SRC-DC8}}}\right) \tag{13}$$

is given by the aperture diameter of the telescope D_{tel} and the distance between Stardust and DC8 $L_{\text{SRC-DC8}}$.

Thus, the radiant power Φ at the entrance aperture of the telescope was obtained as:

$$\Phi = \int_{\Delta\lambda_{\text{pixel}}} M_\lambda \Omega A_{\text{vis}} \tau_{\text{atm}}\, \mathrm{d}\lambda \approx M_\lambda \Omega A_{\text{vis}} \tau_{\text{atm}} \Delta\lambda_{\text{pixel}} \tag{14}$$

The surface temperatures were systematically varied and the emitted radiation was integrated over the whole surface area taking into account the view angle given by the relative positions of DC8 and SRC along the trajectory and multiplied with the solid angle for detection and with the air transmission determined with a ModTran calculation as already shown in Fig. 7 and finally divided by the window transmission of 0.93. Thus, a radiant power at the entrance of the telescope was determined.

Because emission by particles inside the postshock layer is not taken under consideration, these peak temperatures are presently

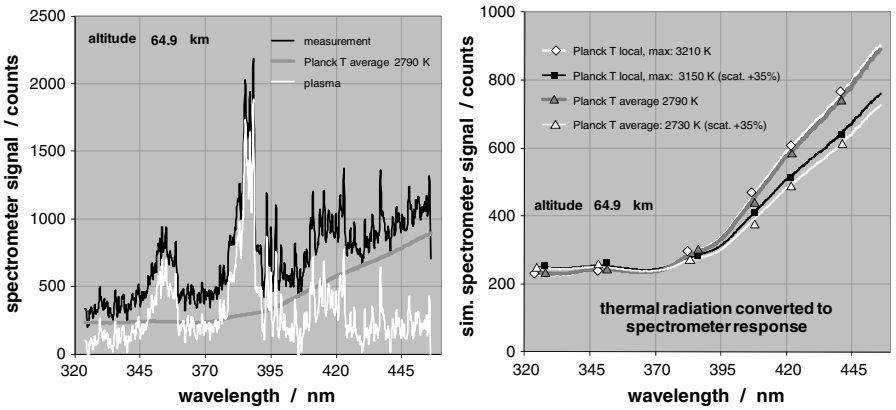

Fig. 10 Measured spectrum, split up into Planck- and plasma-components, for an SRC altitude of 64.9 km close to peak heating and comparison of the spectrometer response to thermal radiation for average and local surface temperatures with and without enhancement of scattered light by 35%. The symbols are only added to distinguish between the different curves and do not indicate preferred data points.

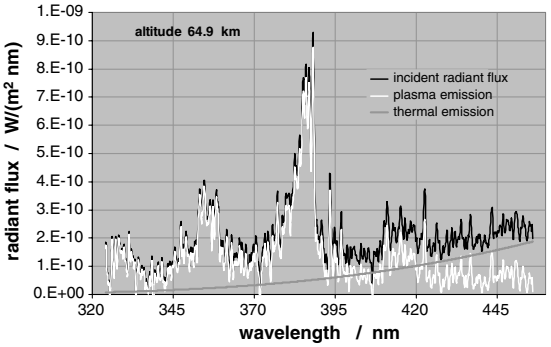

Fig. 11 Emission spectrum at the DC-8 position as combination of thermal radiation of the Stardust heatshield and plasma emission at an altitude of 64.9 km after calibration.

considered to be an upper limit. Inclusion of particle radiation in the analysis will require specification of additional free parameters such as particle size, penetration depth into the boundary layer, particle surface temperature, etc.; these parameters are not known with certainty. Therefore, an implementation of this mechanism at the level of analysis presented here is not useful. Further investigation will require careful examination of the test results presented in [5] and perhaps further ground tests of PICA to determine the necessary parameters.

Figure 10 shows an example for the measured spectrum from the SRC at an altitude of 64.9 km. This spectrum is the most reliable one close to peak heating. Furthermore, the best fitting Planck radiation and the resulting plasma spectrum (which is the difference between measurement and Planck) are displayed. As discussed earlier, discrepancies between calibration during the observation and recalibration in the ground laboratory due to scattered light below 400 nm remain to be reconciled. Therefore, results with unmodified and enhanced scattering are processed in parallel. The results are shown in the right hand part of Fig. 10. With scattering enhanced by 35% a slightly lower surface temperature is obtained, but the maximum difference does not exceed 60 K. Because the qualitative agreement with the measured spectra is slightly better without enhancement of scattered light, the following results are based on the spectrometer response with unmodified scattered light. Surprisingly, the spectral shape of the spectrometer response for constant surface temperatures and the temperature distribution is nearly the same in the wavelength range of interest.

The plasma spectrum extracted from this comparison is now calibrated with the correction factor shown in Fig. 6. The total radiation is computed as the sum of calibrated plasma spectrum and simulated thermal radiation without influences of scattered light as shown in Fig. 11 at an altitude of 64.9 km in units of radiant flux through the aperture of the telescope.

The results are in good agreement with those obtained by the ASTRO [24] and the Echelle [25] instruments which were also used in the Stardust observation campaign. Figure 12 shows the SLIT spectrum and the extrapolation of the thermal emission into the VIS–NIR range and the Echelle data at an altitude of 69.7 km. Upper and lower margins for the thermal emission for a temperature difference of ±50 K are added. Note that the analysis of the SLIT data was performed independently from those of the other instruments, and no scaling factors were transferred. The consistency between the independent experiments gives confidence in the measured data.

The temperature extraction procedure was carried out for the most intense spectra and temperatures were achieved over altitude for the two cases of constant SRC temperature and linearized distribution. The upper error bars indicate the uncertainties due to tracking errors if the compensating curve for the upper bound as shown in Fig. 4 is used instead of the actual measurement which brings the values closer to a smooth curve. The lower error bars show the temperatures for the case of scattered light increased by 35% which lowers the temperatures as discussed in Sec. III.C and shown in Fig. 10. In addition to the graph in Fig. 13 which shows a comparison with the results obtained with DPLR, again with averaged and locally resolved temperatures, the experimentally determined temperatures are tabulated in the Appendix.

The CFD temperatures for the averaged temperature assumption are in good agreement with the SLIT results except for the values where the tracking was apparently off (shown as open symbols) as derived from the data shown in Fig. 4. If a temperature distribution is introduced, the DPLR peak values at the SRC tip are substantially higher than the experimentally obtained results by at least 200 K. However, the experimental method for determining the tip temperatures is consistent with the case of constant temperatures and the results agree with the SLIT and Echelle data.

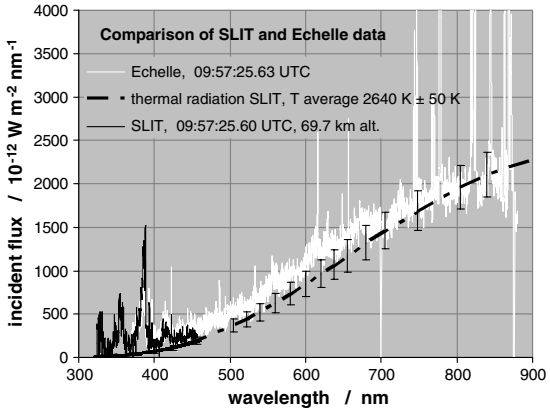

Fig. 12 Comparison of the SLIT spectrum and an extrapolation of the extracted thermal emission to the NIR/VIS with an Echelle spectrum [25] at an altitude of 69.7 km.

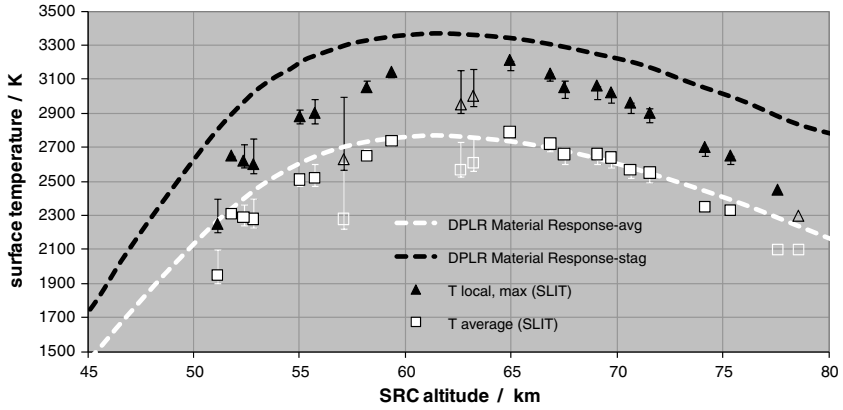

Fig. 13 SRC surface temperatures obtained from SLIT emission spectra and DPLR CFD simulations for the assumption of averaged and locally resolved temperatures. Upper error bars indicate the uncertainty due to tracking errors, the lower ones the uncertainty due to treatment of scattered light.

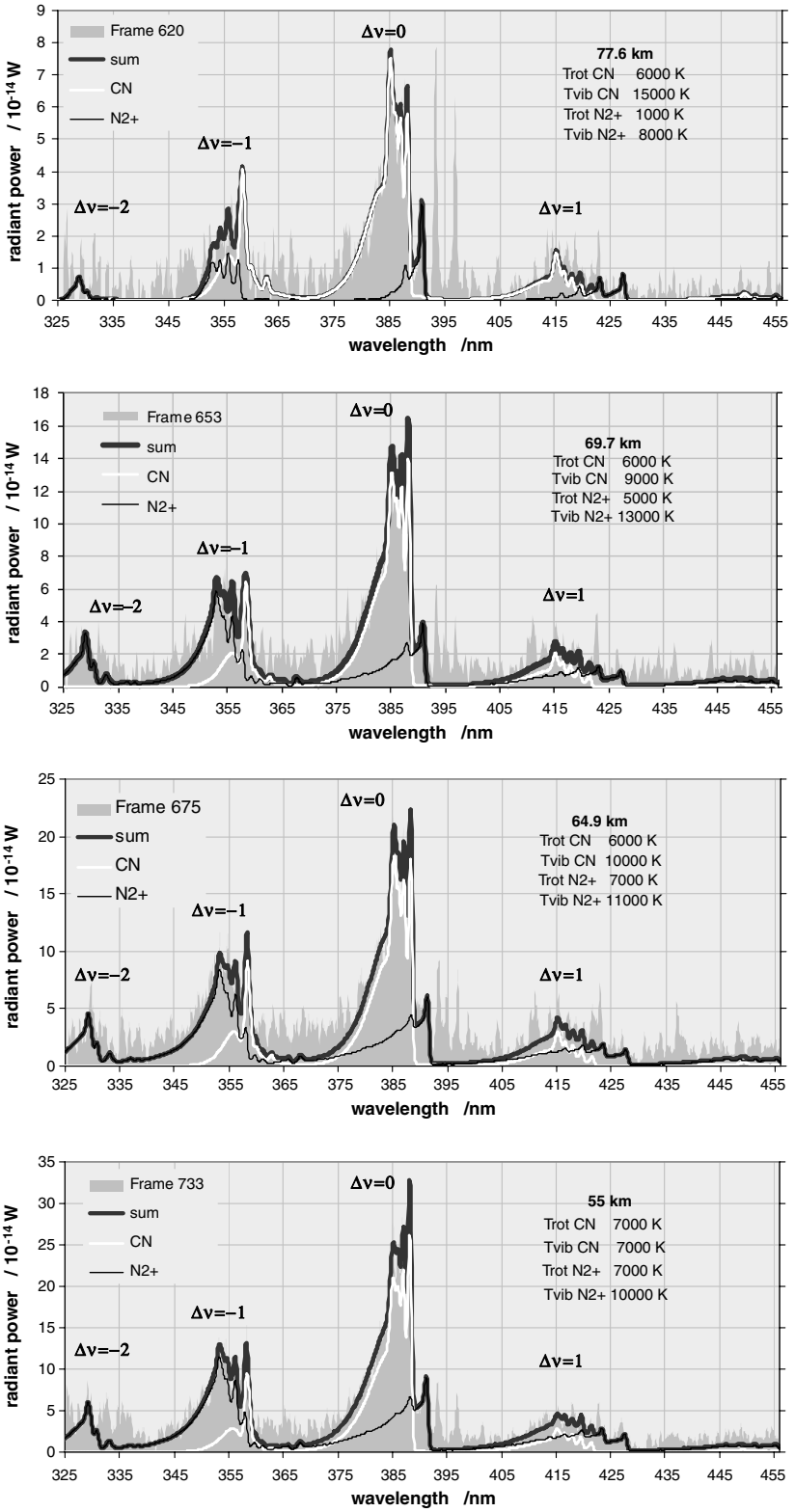

Fig. 14 Measured and simulated emission of CN Violet and N_2^+ first neg. at altitudes of 77.6, 69.7 (comparison with Echelle data), 64.9 (most reliable spectrum close to peak heating), and 55 km before and after peak heating.

B. Analysis of Plasma Spectra

The measured spectra were dominated by the emission of carbon nitride, or CN (CN violet: $B^2\Sigma^+ \rightarrow X^2\Sigma^+$) and N_2^+ (N_2^+ first neg.: $B^2\Sigma_g^+ \rightarrow X^2\Sigma_u^+$). Atomic lines, especially the emission lines of Ca and Ca^+, were clearly identified in all spectra. There was strong evidence of H and O lines before peak heating, but not after. Lines of N could not be identified clearly. A theoretical simulation of the molecular radiation of CN and N_2^+ was carried out using the line-by-line code EMCAL [26] under variation of the rotational and vibrational temperatures between 1000 and 20,000 K. Rotational and vibrational temperatures define the shape of the molecular bands and therefore can be determined without knowing the absolute number densities of electronically excited levels, which are most likely in nonequilibrium. The temperatures which originated the best fitting spectra are considered to be the effective rotational and vibrational temperatures. In that sense effective shall express the fact that, again,

spatial variations of temperature in the postshock layer have been neglected in this process. In Fig. 14 the best fits for the emission of CN Violet and N_2^+ first neg. at altitudes of 77.6 km as one of the first SLIT spectra, 69.7 km in the overlapping regime with Echelle data, 64.9 km as the most reliable spectrum close to peak heating, and 55 km as example after peak heating are shown. The $\Delta\nu = 0$, $\Delta\nu = 1$, and $\Delta\nu = -1$ bands of both species are clearly visible which enables an extraction of vibrational temperature. In addition, the $\Delta\nu = -2$ band of N_2^+ is seen. Simulation and measurement show reasonable agreement which improves with decreasing altitude. However, strong scattering is seen in the data, particularly at high altitudes, which might also be emission due to other molecules and atoms which are not yet identified.

If these fits are applied to all spectra, temperature distributions of N_2^+ and CN can be determined along the trajectory. The vibrational temperature of CN is found to be lower than that of N_2^+. However, the rotational temperatures are quite close at altitudes below 67 km. In fact, the region with the most effective combination of particle density of the species of concern and underlying temperature will dominate the emitted spectrum. For all measured spectra, CN rotational temperatures are around 7000 K. This temperature is clearly higher than the plasma temperature in the boundary layer close to the surface. CN that is produced close to the surface would have to diffuse through the boundary layer into the postshock region in a sufficient amount to generate molecular emission at the deduced rotational temperatures. Another possibility is that particles from microspallation of the heatshield might penetrate the postshock region. Thus, CN would be produced in the hot region by erosion of these particles yielding emission at the observed temperatures. Further work is needed to check these assumptions. N_2^+ is mainly formed in the postshock layer. This means that the major contributions for the different radiating species in the same spectrum may be produced in different regions of the flowfield. Because of the integration over the whole flowfield, the temperatures values have probably only limited relevance. However, they are necessary to compute the integrated value of the radiance emitted by the first neg. systems of CN and N_2^+ as the integral of the simulated spectra in the detected wavelength range between 325 and 456 nm divided by the corresponding solid angle. A direct integration over experimental spectra would not allow for a separation of these systems. Furthermore, issues with a superposition of other radiating species would introduce new errors. The integral value over the simulated radiation as shown in Fig. 15 might be easier to handle for further analysis using CFD simulation than the single spectra; the numerical values are tabulated in the Appendix. Compensating curves are plotted for both species to illustrate the general characteristic with SRC altitude. Values which were clearly below these compensating curves are marked by open symbols and are only displayed for the sake of completeness. The scatter in the values is clearly related to the overall intensity on the CCD and therefore to errors in tracking. In addition, predicted radiative and convective (divided by 10 for better visibility) heat fluxes [21] are plotted. Both N_2^+ and CN emission seem to reach maximum before peak heating, although reliable data points are available only shortly before and after peak heating. The time history of the N_2^+ emission follows the predicted radiative heat flux quite well. The trend CN emission compared with its peak value is clearly higher than the corresponding value of the radiative heat flux before peak heating and resembles more the convective heat flux history although shifted to higher altitudes. However, after peak heating, the CN emission decreases as quickly as the N_2^+ emission and the predicted radiative heat flux.

One possible interpretation is that in early reentry, CN emission is mainly determined by ablation while after peak heating, CN emission is dominated by the plasma properties. This might indicate that in the latter case CN is mainly generated in the hot plasma region, as it would be if CN were generated by particles that spall from the heatshield. For further interpretation, a spectral simulation should be performed on the basis of spatially resolved CFD results. A confirmation of this assumption would entail comparison with measured spectra. However, such a spectral simulation with PARADE [27] based on URANUS [28] CFD computations of the flowfield around Stardust did not show satisfying results mainly due to the fact that CN was not present in the flowfield solver and that N_2^+ existed only in very low concentrations. Therefore, the two strongest radiators were not covered at all or only with a high factor of uncertainty. At present, no reliable alternative is available that would take account of the special variation of temperatures and particle densities in the flowfield. Recent predictions [29] of the plasma properties show some promise. These simulations might be the basis for more accurate data evaluation.

VI. Conclusions

The emission of postshock and surface radiation during the Stardust reentry was detected during a NASA-led mission aboard the Agency's DC-8 airborne observatory. Spectra were taken in the wavelength range from 324 to 456 nm with a pixel resolution of 0.08 nm, and with a measurement frequency of 5 Hz during 30 s around the point of maximum heating. Because of the difficulties in tracking, not every spectrum contained data. Nevertheless, the emission of CN as a major ablation product as well as N_2^+ and different atoms could be monitored successfully during that time. Because of the nature of the setup, no spatial resolution of the radiation data was achieved. Therefore, all measured values represent an integration both over the visible part of the glowing heatshield and over the plasma in the postshock region. The measured spectra could be split up into continuum spectra, which represent a superposition of the heatshield radiation and the continuum radiation of particles due to microspallation of the heatshield material in the plasma, and into line spectra from the plasma in the postshock layer. Influence of

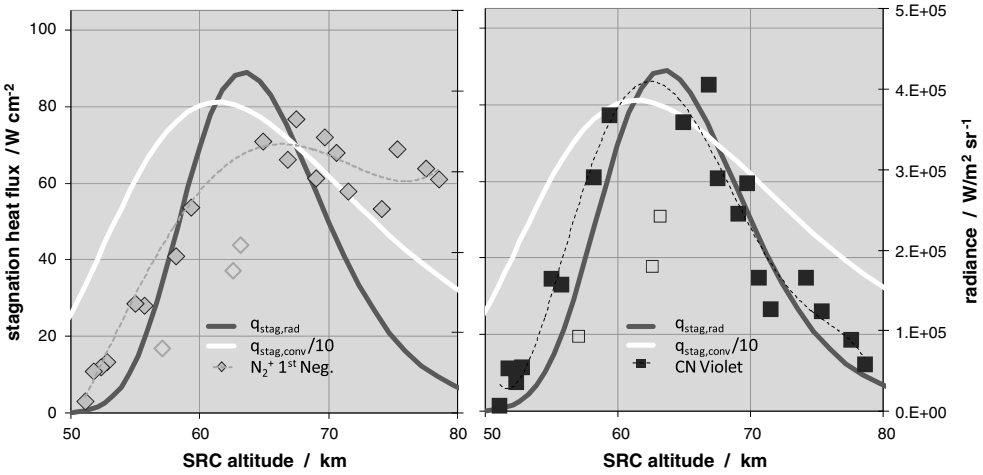

Fig. 15 Spatially integrated, emitted radiance of the first neg. system of N_2^+ and the CN Violet integrated in the wavelength range between 325 and 456 nm and predicted radiative and convective stagnation heat fluxes [21] vs SRC altitude.

scattered light during the calibration measurements was significant and corrected for by a recalibration. From the continuum spectra, Planck temperatures were determined under the assumption of constant SRC surface temperatures, and for a temperature distribution whose shape was approximated to a CFD solution with DPLR. The orientation of the SRC relative to the DC8 yielding information on the visible surface and viewing factors as well as the varying distance and atmospheric transmission were taken into account. So far, contributions of glowing dust particles in the surrounding plasma are not included yet. The key results are:

1) Intensity corrected emission spectra provide a data basis along the trajectory at altitudes from 77 to 52 km. The good agreement with data obtained independently from the Echelle spectrometer in the same observation campaign enhances confidence in both SLIT data acquisition and analysis.

2) SRC heatshield temperatures deduced from the experimental data (assuming constant temperatures across the heatshield surface) are in good agreement with results from DPLR CFD analysis. The extrapolation of the thermal radiation to Echelle wavelengths yields error estimates on the order of ± 50 K for data points where the was in the center of the flied of view. An estimate of the uncertainties introduced by tracking errors was performed by a comparison with temperatures determined from an upper bound compensating curve determined by the spectra where tracking was good. If a temperature distribution is assumed, the peak temperatures from the experimental data are constantly lower by about 200 K than the corresponding CFD results.

3) Rotational temperatures of N_2^+ and CN were obtained from a scaled comparison with simulated spectra. However, these temperatures are only averaged values over the whole flowfield. Therefore, they were only used for the computation of spectrally integrated emission of these two species. The time history of the emitted radiance of the N_2^+ first neg. system agrees quite well with the predictions of radiative stagnation heat flux. CN emission at high altitudes, in reference to its peak emission, is stronger and resembles the time evolution of convective heat flux. A possible conclusion is that CN emission is characteristic for surface ablation in early reentry while it might be dominated by plasma characteristics after peak heating. This emission may be used for a future comparison with CFD data.

Further interpretation of measured emission spectra would require flowfield solutions which include ablation products (in particular CN) coupled to a radiation code. Thus, more accurate comparisons with the experimental data should be possible through an integration over the spatially resolved CFD data. For future missions, a simultaneous optical measurement of plasma properties through on board instrumentation in combination with an airborne observation is proposed to enhance the accuracy of the results by providing additional information on spatial distributions.

Appendix: A

The surface temperatures determined from the measured spectra are considered one major results of this work. To ease a comparison with other works, the numerical values are given in Table A1 vs SRC altitude and time from entry interface (EI). For the simplified temperature distribution, the peak temperature $T_{\text{local,tip}}$. the temperature at 5 cm axial distance to the tip (here occurs the coupling between the two straight lines) $T_{\text{local,5 cm}}$ and the temperature at 20 cm axial distance to the tip (edge of the heatshield) $T_{\text{local,edge}}$ are given. In addition to the surface temperatures, the emission of the two major molecular radiators CN and N_2^+ from the CN Violet ($B^2\Sigma^+ \rightarrow X^2\Sigma^+$) and the N_2^+ 1st Neg. ($B^2\Sigma_g^+ \rightarrow X^2\Sigma_u^+$) systems seem to be suitable for a future comparison with numerical simulation. Therefore, the radiances of these two systems, integrated between 324.38 and 456.52 nm as described in Sec. V are listed as well. Following the notation in Figs. 9 and 15, values where the tracking was obviously off are included but printed in gray color.

Acknowledgments

Preparation of the measurement campaign and first evaluation took place at the Institut für Raumfahrtsysteme of the Universität Stuttgart. The authors wish to thank all IRS members who were involved, in particular, Georg Herdich, as well as Monika Auweter-Kurtz for her continued support, and Markus Pietras, Ricarda Wernitz, and Haida Abdennabi for contributions during conception and first evaluation, and Thiemo Knigge and Maria von Schönermark for providing the ModTran data. The authors wish to acknowledge DLR, German Aerospace Center and the Steinbeis Transferzentrum Plasma- und Raumfahrttechnologie for funding the development of SLIT and the observation itself, and to LOT-Oriel/Andor for providing the EMCCD camera. Furthermore, the authors also wish to thank NASA for the opportunity to participate in this mission, as well as to the NASA Engineering and Safety Center for funding the observation mission in general. The whole mission would not have been possible without the support of the ground crew at NASA Ames Research Center or without the great performance of the DC-8 crew. Thanks also to Peter Jenniskens from SETI Institute for the coordination of the mission. Finally, thanks to Dinesh Prabhu,

Table A1 SRC surface temperatures as determined from SLIT data under the assumption of a constant surface temperature and a simplified temperature distribution given by two straight lines

Time since EI, s	Altitude, km	T_{average}, K	$T_{\text{local,tip}}$, K	$T_{\text{local,5 cm}}$, K	$T_{\text{local,edge}}$, K	CN violet W m^{-2} sr^{-1}	N_2^+ first neg. W m^{-2} sr^{-1}
35.9	78.59	2100	2300	2029	1909	2.90E + 05	5.86E + 04
36.7	77.58	2100	2450	2162	2034	3.04E + 05	8.85E + 04
38.5	75.35	2330	2650	2338	2200	3.28E + 05	1.25E + 05
39.5	74.14	2350	2700	2382	2241	2.53E + 05	1.66E + 05
41.7	71.54	2550	2900	2559	2407	2.75E + 05	1.27E + 05
42.5	70.62	2570	2960	2612	2457	3.23E + 05	1.66E + 05
43.3	69.72	2640	3020	2665	2507	3.43E + 05	2.83E + 05
43.9	69.05	2660	3060	2700	2540	2.91E + 05	2.46E + 05
45.1	67.50	2660	3050	2691	2532	3.65E + 05	2.89E + 05
45.9	66.84	2720	3130	2762	2598	3.15E + 05	4.05E + 05
47.7	64.93	2790	3210	2832	2664	3.37E + 05	3.59E + 05
49.5	63.2	2610	3000	2647	2490	2.08E + 05	2.43E + 05
50.1	62.61	2570	2950	2603	2449	1.76E + 05	1.80E + 05
53.7	59.35	2740	3140	2771	2606	2.55E + 05	3.68E + 05
55.1	58.18	2650	3050	2691	2532	1.95E + 05	2.91E + 05
56.5	57.07	2280	2630	2321	2183	7.99E + 04	9.29E + 04
58.3	55.73	2520	2900	2559	2407	1.33E + 05	1.58E + 05
59.3	55.02	2510	2880	2541	2390	1.36E + 05	1.64E + 05
62.7	52.83	2280	2600	2294	2158	6.31E + 04	5.49E + 04
63.5	52.36	2290	2620	2312	2175	5.66E + 04	3.59E + 04
64.5	51.79	2310	2650	2338	2200	5.15E + 04	5.37E + 04
65.7	51.14	1950	2250	1985	1868	1.42E + 04	6.90E + 03

ELORET Corporation, for discussion and comments, David Saunders, ELORET Corporation, for data on effective surface areas which was used to independently cross-check the values used in the present work, and to the reviewers for their detailed and valuable suggestions.

References

[1] Desai, P. N., Mitcheltree, R. A., and Cheatwood, F. McNeil, "Entry Trajectory Issues for the Stardust Sample Return Capsule," *International Symposium on Atmospheric Reentry Vehicles and Systems*, Association Aeronautique & Astronautique de France, Paris, 1999.

[2] "Stardust Hypervelocity Entry Observing Campaign Support," NASA Engineering and Safety Center Rept. RP-06-80, Aug. 2006.

[3] Jenniskens, P., Kontinos, D., Jordan, D., Wright, M., Olejniczak, J., Raiche, G., Wercinski, P., Desai, P. N., Taylor, M. J., Stenbaek-Nielsen, H. C., McHarg, M. G., Abe, S., Rairden, R. L., Albers, J., Winter, M., Harms, F., Wolf, J., ReVelle, D. O., Gural, P., Dantowitz, R., Rietmeijer, F., Hladiuk, D., and Hildebrand, A. R., "Preparing for the Meteoric Return of Stardust," *Workshop on Dust in Planetary Systems*, SP-643ESA, Noordwijk, The Netherlands, 2005.

[4] Jenniskens, P., Jordan, D., Kontinos, D., Wright, M., Olejniczak, J., Raiche, G., Wercinski, P., Schilling, E., Taylor, M., Rairden, R., Stenbaek-Nielsen, H., McHarg, M. G., Abe, S., and Winter, M., "Preliminary Results from Observing the Fast Stardust Sample Return Capsule Entry in Earth's Atmosphere on January 15, 2006," Progress in Planetary Exploration Missions, *26th Meeting of the IAU*, International Astronomical Union, Paris, 2006.

[5] Raiche, G. A., and Driver, D. M., "Shock Layer Optical Attenuation and Emission Spectroscopy Measurements During Arc Jet Testing with Ablating Models," *Proceedings of the 42th AIAA Aerospace Sciences Meeting and Exhibit*, AIAA Paper 2004-825, 2004.

[6] Park, C., Raiche, G. A., and Driver, D. M., "Radiation of Spalled Particles in Shock Layers," *Proceedings of the 42th AIAA Aerospace Sciences Meeting and Exhibit*, AIAA Paper 2004-1349, 2004.

[7] Winter, M., and Herdrich, G., "Spectroscopic Observation of the Stardust Re-Entry in the Near UV," *39th AIAA Thermophysics Conference*, AIAA Paper 2007-4050, 2007.

[8] Bernstein, L. S., Berk, A., Acharya, P. K., Robertson, D. C., Anderson, G. P., Chetwynd, J. H., and Kimball, L. M., "Very Narrow Band Model Calculations of Atmospheric Fluxes and Cooling Rates," *Journal of the Atmospheric Sciences*, Vol. 53, No. 20, 1996, pp. 2887–2904. doi:10.1175/1520-0469(1996)053<2887:VNBMCO>2.0.CO;2

[9] Anderson, G. P., Berk, A., Acharya, P. K., Matthew, M. W., Bernstein, L. S., Chetwynd, J. H., Dothe, H., Adler–Golden, S. M., Ratkowski, A. J., Felde, G. W., Gardner, J. A., Hoke, M. L., Richtsmeier, S. C., Pukall, B., Mello, J., and Jeong, L. S., "MODTRAN4: Radiative Transfer Modeling for Remote Sensing," *Algorithms for Multispectral, Hyperspectral, and Ultraspectral Imagery VI*, Vol. 4049, edited by Sylvia S. Chen, Michael R. Descour, SPIE, Bellingham, WA, 2000, pp. 176–183.

[10] MacCormack, R., and Candler, G., "The Solution of the Navier-Stokes Equations Using Gauss–Seidel Line Relaxation," *Computers and Fluids*, Vol. 17, No. 1, 1989, pp. 135–150. doi:10.1016/0045-7930(89)90012-1

[11] Yee, H., "A Class of High-Resolution Explicit and Implicit Shock Capturing Methods," NASA TM 101088, Feb. 1989.

[12] Millikan, R., and White, D., "Systematics of Vibrational Relaxation," *Journal of Chemical Physics*, Vol. 39, No. 12, 1963, pp. 3209–3213. doi:10.1063/1.1734182

[13] Park, C., *Nonequilibrium Hypersonic Aerothermodynamics*, Wiley, New York, 1990.

[14] Parker, J. G., "Rotational and Vibrational Relaxation in Diatomic Gases," *Physics of Fluids*, Vol. 2, No. 4, 1959, pp. 449–462. doi:10.1063/1.1724417

[15] Gupta, R., Yos, J., Thompson, R., and Lee, K., "A Review of Reaction Rates and Thermodynamic and Transport Properties for an 11-Species Air Model for Chemical and Thermal Nonequilibrium Calculations to 30,000 K," NASA RP-1232, Aug. 1990.

[16] Bartlett, E. P., Kendal, R. M., and Rindal, R. A., "An Analysis of the Coupled Chemically Reacting Boundary Layer and Charring Ablator: Part IV: A Unified Approximation for Mixture Transport Properties for Multi-Component Boundary-Layer Applications," NASA CR-1063, June 1968.

[17] Hirschfelder, J. O., Curtiss, C. F., and Bird, R. B., *Molecular Theory of Gases and Liquids*, Wiley, New York, 1964.

[18] Desai, P., Qualls, G., and Levit, C., "Stardust Entry Reconstruction," AIAA Paper 2008-1198, Reno, NV, 2008.

[19] Milos, F. S., Chen, Y.-K., and Squire, T. H., "Updated Ablation and Thermal Response Program for Spacecraft Heatshield Analysis," NASA Paper TFAWS06-1008, August 2006.

[20] Milos, F. S., and Chen, Y.-K., "Two-Dimensional Ablation, Thermal Response and Sizing Program for Charring Ablators," *46th AIAA Aerospace Sciences Meeting*, AIAA Paper 2008-1223, 2008.

[21] Liu, Y., Prabhu, D., Trumble, K., Saunders, D., and Jenniskens, P., "Radiation Modeling for the Reentry of the Stardust Sample Return Capsule," AIAA Paper 2008-1213, 2008.

[22] Olynick, D., Chen, Y. K., and Tauber, M. E., "Aerothermodynamics of the Stardust Sample Return Capsule," *Journal of Spacecraft and Rockets*, Vol. 36, No. 3, May–June 1999, pp. 442–462. doi:10.2514/2.3466

[23] Tran, H. K., Johnson, C. E., Rasky, D. J., Hui, F. C., Hsu, M., and Chen, T., "Phenolic Impregnated Carbon Ablators (PICA) as Thermal Protection Systems for Discovery Missions," NASA Technical Memorandum 110440, April 1997.

[24] Jenniskens, P., Wilson, M. A., Laux, C. O., and Winter, M., "High Resolution Spectroscopy of the Stardust Sample Return Capsule Entry at Peak Heating with ASTRO," *Journal of Spacecraft and Rockets*, Vol. 47, No. 5, pp. 718–735.

[25] Jenniskens, P., "Resolved CN Band Profile of Stardust Capsule Radiation at Peak Heating," *Journal of Spacecraft and Rockets*, Vol. 47, No. 6, pp. 873–877. doi:10.2514/1.38074

[26] Winter, M., "Emission Spectroscopic Investigation of the Flow Field Around a Blunt Body in a High Enthalpy Flow," Ph.D. Dissertation, Universität Stuttgart, Stuttgart, Germany, Dec. 2006 (in German).

[27] Winter, M., Pfeiffer, B., Fertig, M., Auweter-Kurtz, M., and Smith, A. J., "Recent Status of the Plasma Radiation Database PARADE," *Proceedings of the AIAA Thermophysics Conference*, AIAA Paper 2004-2376, 2004.

[28] Fertig, M., Dohr, A., and Frühauf, H.-H., "Transport Coefficients for High Temperature Nonequilibrium Air Flows," *Journal of Thermophysics and Heat Transfer*, Vol. 15, No. 2, 2001, pp. 148–156.

[29] Ozawa, T., Zhong, J., Levin, D. A., Bogerz, D., and Wright, M., "Modeling of the Stardust Reentry Flows with Ionization in DSMC," *Proceedings of the 45th AIAA Aerospace Sciences Meeting and Exhibit*, AIAA, Reston, VA, 2007.

M. Wright
Guest Editor